Spatiotemporal mode-selective quantum frequency converter

Santosh Kumar,* He Zhang, Prajnesh Kumar, Malvika Garikapati, Yong Meng Sua, and Yu-Ping Huang†
Department of Physics, Stevens Institute of Technology, Hoboken, NJ, 07030, USA
and Center for Quantum Science and Engineering, Stevens Institute of Technology, Hoboken, NJ, 07030, USA

(Received 31 May 2021; accepted 26 July 2021; published 6 August 2021)

We experimentally demonstrate a mode-selective quantum frequency converter over a compound spatiotemporal Hilbert space. We show that our method can achieve high extinction for high-dimensional quantum state tomography by selectively upconverting the signal modes with a modulated and delayed pump. By preparing the pump in optimized modes through adaptive feedback control, selective frequency conversion is demonstrated with up to 30 dB extinction. The simultaneous operations over high-dimensional degrees of freedom in both spatial and temporal domains can serve as a viable resource for photon-efficient quantum communications and computation.

DOI: 10.1103/PhysRevA.104.023506

I. INTRODUCTION

High-dimensional (HD) quantum information carriers have been studied with superconducting circuits [1], atomic ensembles [2–4], photons [5,6], and so on. They can increase the information capacity, improve the noise resistance, and make the quantum cryptographic schemes more difficult to hack despite errors [7,8]. In photonic systems, single photons can carry quantum information in an HD Hilbert space subtending polarization, spatial, temporal, frequency, and path degrees of freedom (DOF), with broad applications in long-distance quantum communication, quantum key distribution, quantum gate operations, and quantum teleportation [9–14].

Meanwhile, in modern quantum information architectures, quantum frequency conversion (QFC) has become an essential element with numerous applications in quantum communications and quantum information processing [15,16]. It allows us to convert the frequency of the photons without disturbing their quantum properties [17]. Through QFC, quantum information can be transmitted through optical fiber links using a telecom wavelength at low loss while interfaced with quantum atomic memories [18–20]. Many previously studied nonlinear optics-based QFCs have been demonstrated in two-dimensional Hilbert space for qubit teleportation and communications [21–25]. Recently, this study has been extended to an HD Hilbert space using spatial, frequency, or temporal DOF due to its potential in long-distance quantum communications [26–28]. For example, HD QFC was demonstrated for orbital angular momentum (OAM) qudits via sum frequency generation (SFG) with a flattop Gaussian pump beam [29]. The HD quantum information of the single photons was shown to be transferred from the polarization DOF to the orbital angular momentum DOF and orbital angular momentum to temporal DOF or vice versa [30–32].

In view of the two vivid directions of pursuit, in this paper, we propose and experimentally demonstrate an HD mode-selective QFC in a compound spatiotemporal Hilbert space. The combined spatial and temporal DOF can be realized in a simple experimental setup using a spatial light modulator (SLM) and optical delay line (ODL). We show that the mutually unbiased basis (MUB) sets in an HD Hilbert space can be selectively upconverted according to their spatial and temporal modes. In contrast to previous demonstrations [29], we use an optimized pump beam which is the superposition of many higher-order orthogonal modes. The optimization is performed by using an adaptive feedback technique [33]. Our HD mode-selective QFC provides an ingenious and effective solution for quantum information processing using single photons in HD Hilbert spaces, with potential applications in quantum communication and quantum networks [34–36]. In the future, it can be extended to hyperentangled photon generation for promising quantum applications [37–40].

II. MODEL

We consider a signal and a pump beam in the spatiotemporal domain as

$$\Psi_{i\equiv p,s}(x,y,z,t) = A_i E_i^r(x,y,z) E_i^t(t) \exp[-i(k_i z - \omega_i t)], \quad (1)$$

where $A_{i\equiv p,s}$ is the input electric-field amplitude, and $E_i^r(x,y,z)$ and $E_i^t(t)$ are the electric fields in the spatial and temporal domain, respectively. Here, we consider that the full electric field is the product of the spatial and temporal DOF, i.e., we ignore the intercoupling of the space and time DOF [41,42]. Under the slowly varying envelope approximation with negligible group velocity dispersion, the coupled wave differential equations can be written as

$$2ik_s(\partial_z + \beta_s'\partial_t)\Psi_s + \left(\partial_x^2 + \partial_y^2\right)\Psi_s = -2\frac{\omega_s^2}{c^2}\chi\Psi_p^*\Psi_f e^{i\triangle kz}, \quad (2)$$

$$2ik_p(\partial_z + \beta_p'\partial_t)\Psi_p + \left(\partial_x^2 + \partial_y^2\right)\Psi_p = -2\frac{\omega_p^2}{c^2}\chi\Psi_s^*\Psi_f e^{i\triangle kz}, \quad (3)$$

$$2ik_f(\partial_z + \beta_f'\partial_t)\Psi_f + \left(\partial_x^2 + \partial_y^2\right)\Psi_f = -2\frac{\omega_f^2}{c^2}\chi\Psi_p\Psi_s e^{-i\triangle kz}, \quad (4)$$

*skumar5@stevens.edu
†yhuang5@stevens.edu

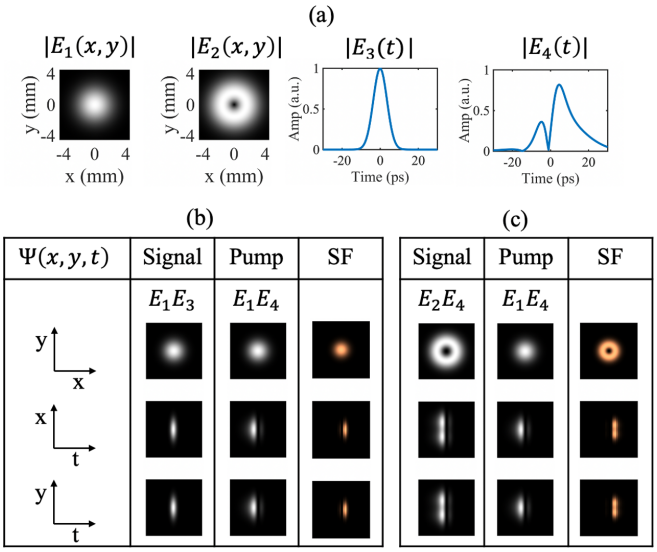

FIG. 1. Generated spatiotemporal SF modes. (a) shows the electric-field amplitude in the spatial and temporal domain for composing different signal and pump modes. (b) SF output for signal mode $\Psi_s = E_1E_3$ with pump mode $\Psi_p = E_1E_4$. (c) SF output for signal mode $\Psi_s = E_2E_4$ with pump mode $\Psi_p = E_1E_4$.

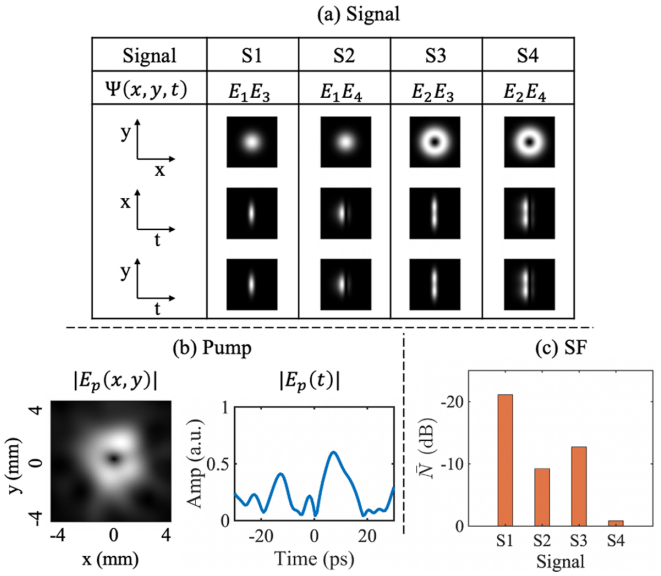

FIG. 2. An example of selection among different spatiotemporal modes S_k ($k = 1, 2, 3, 4$). (a) Four different spatiotemporal modes S_1, S_2, S_3, and S_4, where the spatial and temporal components are shown in Fig. 1(a). (b) The optimized pump mode in the spatial and temporal domain. (c) Normalized SF photon for different signal modes with an optimized pump mode.

where $\beta'_{i=s,p,f}$ and ω_i are the inverse group velocities, and frequencies of the signal, pump, and SF light, respectively. $k_s = n_s\omega_s/c$, $k_p = n_p\omega_p/c$, and $k_f = n_f\omega_f/c$ are their wave numbers. χ is the second-order nonlinear susceptibility. $\Delta k = k_s + k_p - k_f - 2\pi/\Lambda$ is the momentum mismatching condition, where Λ is the poling period of the nonlinear crystal. Equations (2)–(4) can be solved numerically using the split-step Fourier method with an adaptive step size [33,43].

Figure 1 shows an example of the simulated SF output for two different signal modes in the combined spatial and temporal domain. Both signals are converted by the same spatiotemporal pump field. Figure 1(a) plots the electric-field amplitudes in the spatial and temporal domain. These amplitudes are used to create the spatiotemporal signal and pump fields. Figures 1(b) and 1(c) show the SF output for the signal field $\Psi_{s1} = E_1(x,y)E_3(t)$ and $\Psi_{s2} = E_2(x,y)E_4(t)$ with pump field $\Psi_p = E_1(x,y)E_4(t)$, respectively. $E_1(x,y) = e^{-\frac{x^2+y^2}{W_0^2}}$ and $E_3(t) = e^{-\frac{(t-t_0)^2}{(\tau_0)^2}}$ are the Gaussian electric-field amplitudes in the spatial and temporal domain with widths W_0 and τ_0, respectively. $E_2(x,y)$ is a Laguerre-Gaussian mode with angular mode number $l = 1$ and radial mode number $p = 0$ (see the Appendix). Each plot shows the distribution of the modes in the spatial and temporal domain.

Next, we show that the optimized pump field can selectively upconvert a desired signal mode over other overlapping modes. In general, the optimized pump is considered as a superposition of the higher-order modes. It can be written as

$$P_{\text{opt}} = \left[C_{11}\text{LG}_0^0 + C_{01}\text{LG}_1^0 + \cdots + C_{pl}\text{LG}_l^p(x,y)\right] \times[\tau_1\Phi_1(t) + \tau_2\Phi_2(t) + \cdots + \tau_j\Phi_j(t)], \quad (5)$$

where LG_l^p are the Laguerre-Gaussian modes, Φ_j are the Schmidt decomposed temporal modes, and C_{pl} and τ_j are the normalized coefficients of the spatial and temporal modes, respectively.

For a given optimized pump, we select an ith signal mode among other overlapping modes. We first define the normalized SF photon $\bar{N}_i$ of the ith signal as

$$\bar{N}_i = 10\log_{10}\left(\frac{N_i}{\sum_{i=1}^{n} N_i}\right), \quad (6)$$

where N_i is the measured SF photons of the ith signal mode and n is the total number of signal modes. Note that the input incident photons for each signal mode are equal. The selectivity η between the desired signal mode and other overlapping modes can be defined as

$$\eta = \bar{N}_i - \bar{N}_{j\neq i}, \quad (7)$$

where $\bar{N}_i$ and $\bar{N}_{j\neq i}$ are the normalized SF photons of the desired signal and the other overlapping signal modes, respectively.

Figure 2 shows an example in the simulation to select a signal mode (S_4) with respect to other overlapping signal modes (S_1, S_2, and S_3). For simplicity, we used a random-walk optimization method to optimize the pump field in the spatiotemporal domain [33,43]. We consider four signal modes S_k ($k = 1, 2, 3, 4$), which are composed of two spatial (E_1, E_2) and two temporal (E_3, E_4) electric-field amplitudes, as shown in Fig. 1(a). One optimized pump, shown in Fig. 2(b), is designed to select S_4 and suppress the others simultaneously. With this optimized pump, the normalized upconverted SF outputs for different signals are shown in Fig. 2(c). The selectivity of the signal S_4 against S_1, S_2, and S_3 are 20.2, 8.4, and 11.8 dB, respectively. To further improve the selectivity, we can use a particle-swarm optimization algorithm in the spatial and temporal domain [44].

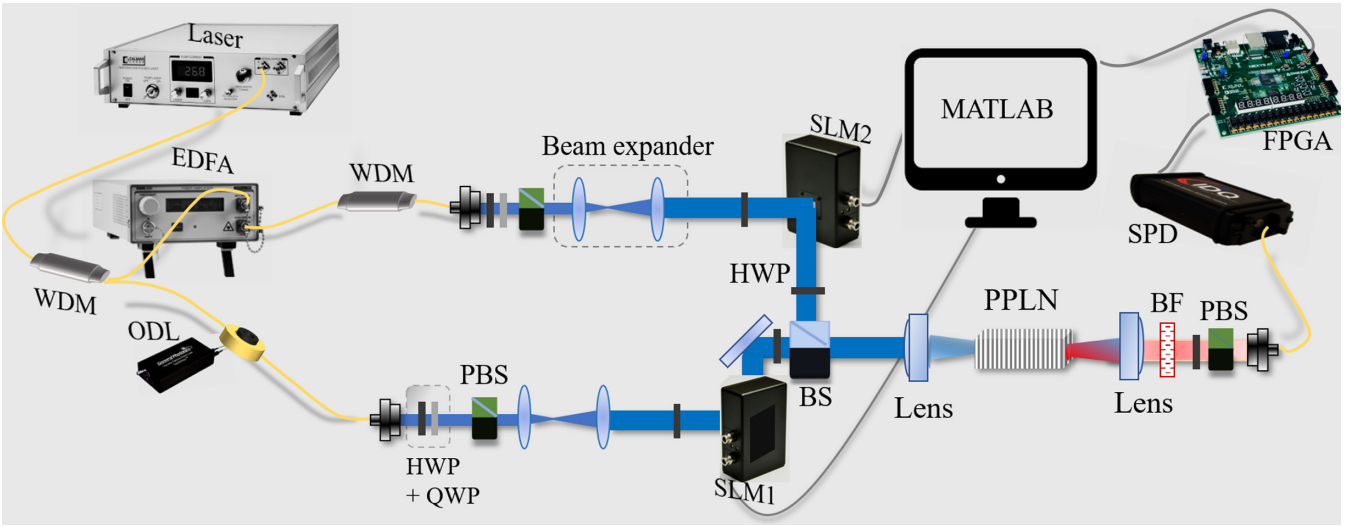

FIG. 3. Experimental setup for high-dimensional mode-selective frequency upconversion process. ODL: programmable optical delay line; SLM: spatial light modulator; BS: beam splitter; WDM: wavelength-division multiplexing; PPLN: magnesium-doped periodic poled lithium niobate crystal; BF: short-pass bandpass filters; and PM: power meter.

III. EXPERIMENTAL SETUP

Figure 3 outlines our present experimental setup. A mode-locked laser is used to generate the pulse train with a pulse width ∼0.3 ps at a 50 MHz repetition rate. We use two inline narrow-band wavelength division multiplexers (WDMs) with a bandwidth of 100 GHz to select two wavelengths, one at 1545 nm as a pump and another at 1558 nm as a signal. A programmable ODL in the signal arm is used to scan the temporal shape of the optical pulses. The pump optical pulses are amplified using an erbium-doped fiber amplifier (Thorlabs, EDFA100S) to obtain a maximum average power ∼10 mW incident on the nonlinear crystal. On the other hand, the signal optical pulses are attenuated with neutral density filters to produce an ultralow optical signal. In free space, both arms select the horizontal polarization for the pump and signal. The transverse full width at half maximum (FWHM) of the pump and signal are 2.8 ± 0.05 and 2.6 ± 0.05 mm, respectively. Then, these two beams are incident on separate spatial-light modulators (Santec SLM-100, 1440 × 1050 pixels, pixel pitch 10.4 × 10.4 μm) [45]. The pump and signal SLMs are used to upload the desired (for example, HG or LG) phase masks. A beam splitter is used to combine the two pulse trains which are focused (focus length $F = 200$ mm) into a temperature-stabilized second-order nonlinear crystal with a poling period of 19.36 μm (5 mol % MgO-doped PPLN, 10 mm length, 3 mm width, and 1 mm height) for the SF generation process. The normalized conversion efficiency of the nonlinear crystal is 1%. It can increase with a high pump laser power and longer crystal length [46]. Half-wave plates on both arms, before the nonlinear crystal, are used to ensure the vertically polarized optical field parallel to the crystal's optical axis. The output pulses are then filtered with a short-pass filter to remove any residual fundamental light and bandpass filters to provide a total >180 dB extinction in rejecting the second harmonic of the pump [43,47]. The visible SF photons pass through a half-wave plate and polarizing beam splitter (PBS). The output SF photons are then coupled into a single-mode fiber (SMF-28) using a fiber collimator consisting of an aspheric lens (Thorlabs A375TM-B). A silicon avalanche photodiode (Si-APD, ID100) is used to detect the photons, which has 15% quantum efficiency. The output of the APD is collected by a field programmable gate array (FPGA, Zedboard ZYNQ-7000) and sent to a computer for postprocessing. A MATLAB program is used to optimize the pump mode using an adaptive feedback technique based on a random-walk optimization [33,44].

IV. RESULTS

Before presenting the results for mode-selective QFC with an optimized pump, we first show the preparation of the quantum states in the spatial HD Hilbert space. For simplicity, we consider small values of azimuthal (l) and radial (p) indices for the Laguerre-Gaussian modes. The upper bound of the indices depends on the beam size, SLM dimension, and cross section of the nonlinear crystal. Figure 4 shows the experimentally measured matrix for the Laguerre-Gaussian signal and pump modes. In this case, both the signal and pump modes have the radial index $p = 0, 1$ and the azimuthal index $l = -3$ to 3. The values in the color bar and matrix represent the normalized SF photon ($\bar{N}$), which is normalized with the sum of the elements in each row (i.e., with the same pump) according to Eq. (6). It is clear from this figure that the angular momenta with opposite signs for the signal and pump modes have a higher extinction compare to other modes. We can also observe that the nearest-neighbor spatial modes are difficult to distinguish [7,33].

Next, we show the manipulation of the generated SF photons by rotating the signal phase mask with respect to the pump phase mask. As an example, in Fig. 5, we plot the simulated and experimentally measured SF photons by rotating the HG_{10} pump and signal masks (see the Appendix for more details). It shows that the SF photons are minimum, when the pump and signal phase masks are orthogonal to each other.

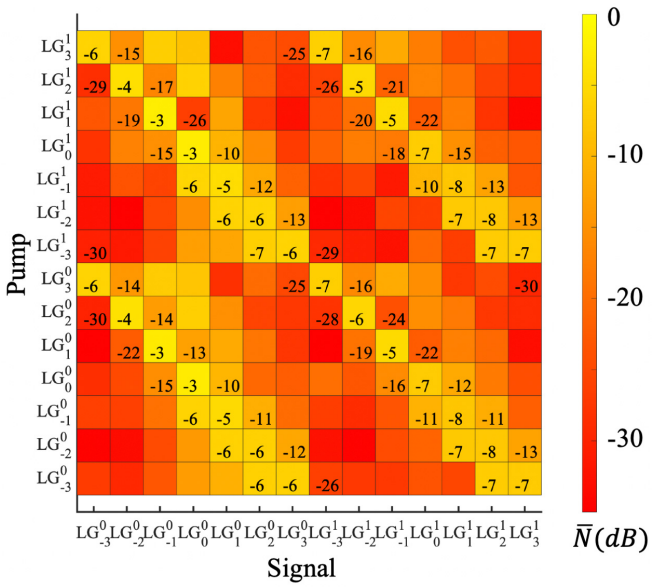

FIG. 4. Measured SF output matrix with higher-order LG modes for the signal and the pump. The values in the matrix are representing the normalized SF output $\bar{N}$ dB [using Eq. (6)].

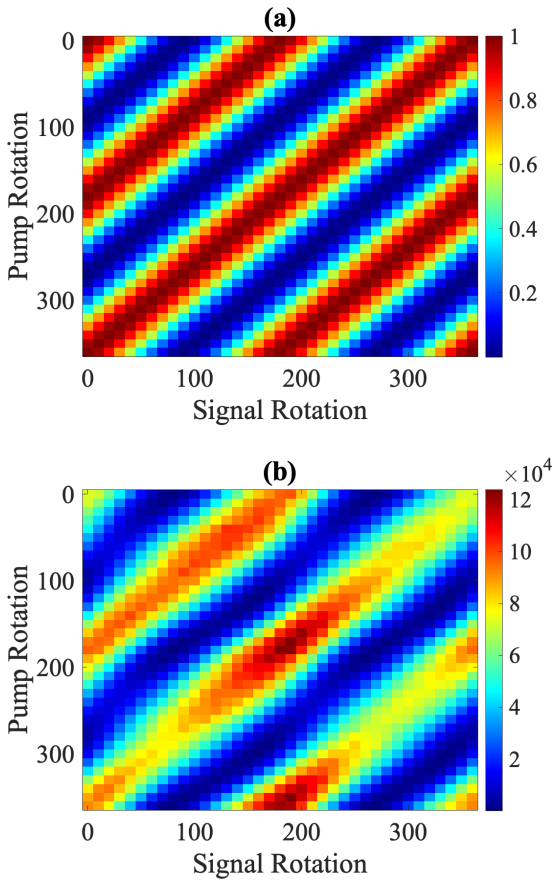

FIG. 5. SF photon counts are plotted by rotating the Hermite-Gaussian (HG_{10}) phase mask of the pump and the signal in (a) simulation and (b) experiment. The simulated result is normalized using the maximum value in the plot. The color bar, shown in (b), represents the detected SF counts.

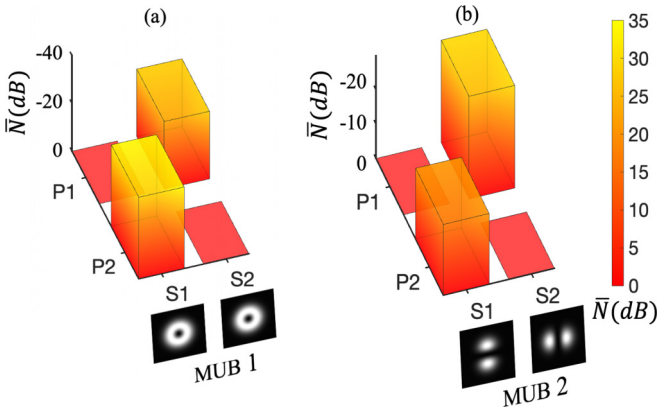

FIG. 6. Qubit tomography for MUB of signal modes: (a) $\{|\mathrm{LG}^0_{+1}\rangle, |\mathrm{LG}^0_{-1}\rangle\}$ and (b) $\{(|\mathrm{LG}^0_{+1}\rangle + |\mathrm{LG}^0_{-1}\rangle)/\sqrt{2}, (|\mathrm{LG}^0_{+1}\rangle - |\mathrm{LG}^0_{-1}\rangle)/\sqrt{2}\}$. Normalization is done by summation of each row. P_1 and P_2 are the optimized pump modes to selectively upconvert signals S_1 and S_2, respectively.

This flexible control of the phase mask rotation can be utilized for the HD quantum applications [48,49].

After that, optimized pump modes are prepared to selectively upconvert the MUB of qubit and qudit states. The optimized pump modes are in the superposition of the 18 higher-order LG modes ($l \in [-5:5]$, $p \in [0,1]$). To show the selectivity for each optimized pump, the upconverted photons are collected and normalized. As an example, in Fig. 6, we use two sets of MUB for the signal qubit states: in Fig. 6(a), $\{|\mathrm{LG}^0_{+1}\rangle, |\mathrm{LG}^0_{-1}\rangle\}$, and in Fig. 6(b), $\{(|\mathrm{LG}^0_{+1}\rangle + |\mathrm{LG}^0_{-1}\rangle)/\sqrt{2}, (|\mathrm{LG}^0_{+1}\rangle - |\mathrm{LG}^0_{-1}\rangle)/\sqrt{2}\}$. The qubit tomography shows that the optimized pump modes can selectively pick up the desired modes. It achieves a selectively of ∼28 dB on average. Similarly, Fig. 7 shows the superposition of four LG modes, i.e., qudit, to prepare two MUB consisting of four signal modes. Figure 7(a) shows the first MUB, and we use signals $\{(|\mathrm{LG}^0_{+1}\rangle + |\mathrm{LG}^0_{-1}\rangle + |\mathrm{LG}^1_{+1}\rangle + |\mathrm{LG}^1_{-1}\rangle)/2, (|\mathrm{LG}^0_{+1}\rangle + |\mathrm{LG}^0_{-1}\rangle - |\mathrm{LG}^1_{+1}\rangle - |\mathrm{LG}^1_{-1}\rangle)/2, (|\mathrm{LG}^0_{+1}\rangle - |\mathrm{LG}^0_{-1}\rangle - |\mathrm{LG}^1_{+1}\rangle + |\mathrm{LG}^1_{-1}\rangle)/2, (|\mathrm{LG}^0_{+1}\rangle - |\mathrm{LG}^0_{-1}\rangle + |\mathrm{LG}^1_{+1}\rangle - |\mathrm{LG}^1_{-1}\rangle)/2\}$ to selectively upconvert each with different optimized pump modes. The selectivity η gives ∼17 dB on average extinction. In Fig. 7(b), we show the second MUB, which consists of four signals $|\mathrm{LG}^0_{+1}\rangle$, $|\mathrm{LG}^0_{-1}\rangle$, $|\mathrm{LG}^1_{+1}\rangle$, and $|\mathrm{LG}^1_{-1}\rangle$. We selectively upconvert these four signals with different optimized pump modes. The value of selectivity η gives ∼16 dB extinction.

Figure 8 demonstrates the selectivity among five higher-order LG modes: in Fig. 8(a), LG^0_0, LG^0_1, LG^0_2, LG^0_3, LG^0_4, and in Fig. 8(b), LG^1_0, LG^1_1, LG^1_2, LG^1_3, LG^1_4 with two different optimized pumps, respectively. Figures 8(a) and 8(b) show the selectivity of signal modes $\{\mathrm{LG}^0_1$ and $\mathrm{LG}^0_2\}$, and $\{\mathrm{LG}^1_1$ and $\mathrm{LG}^1_2\}$ with simultaneously suppressing other overlapping modes. Here also, the selectivity for each optimized pump is determined by the collected and normalized SF photons, as defined in Eq. (7). We can see that the selectivities for five signal modes in Figs. 8(a) and 8(b) are in between 20 and 30 dB and 15 and 25 dB, respectively.

To show the performance of mode-selective QFC in the spatial and temporal domain, we introduce the time-bin

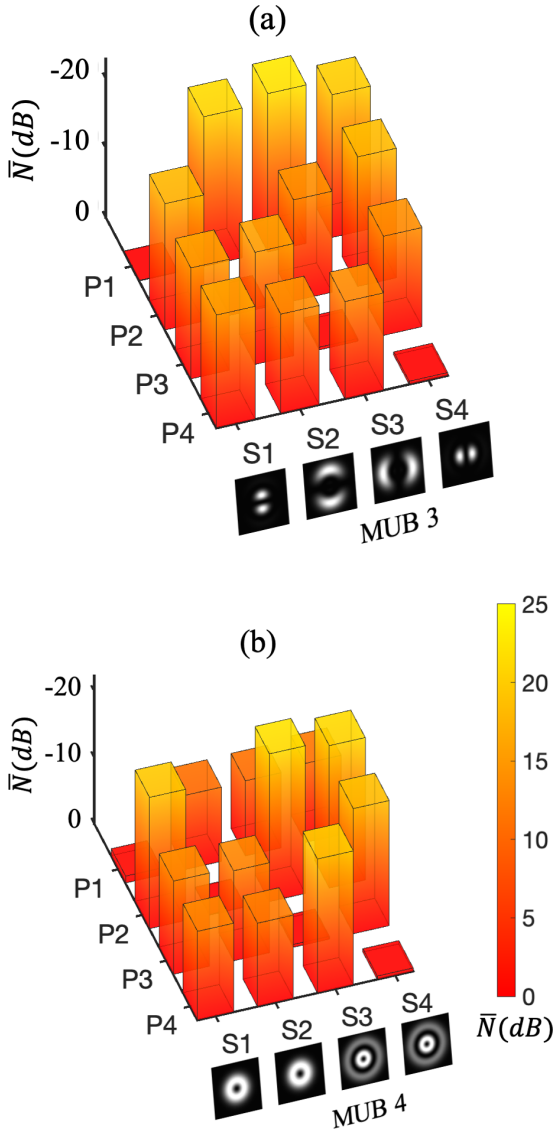

FIG. 7. Qudit tomography for MUB of signal modes: (a) $\{(|\mathrm{LG}^0_{+1}\rangle + |\mathrm{LG}^0_{-1}\rangle + |\mathrm{LG}^1_{+1}\rangle + |\mathrm{LG}^1_{-1}\rangle)/2$, $(|\mathrm{LG}^0_{+1}\rangle + |\mathrm{LG}^0_{-1}\rangle - |\mathrm{LG}^1_{+1}\rangle - |\mathrm{LG}^1_{-1}\rangle)/2$, $(|\mathrm{LG}^0_{+1}\rangle - |\mathrm{LG}^0_{-1}\rangle - |\mathrm{LG}^1_{+1}\rangle + |\mathrm{LG}^1_{-1}\rangle)/2$, $(|\mathrm{LG}^0_{+1}\rangle - |\mathrm{LG}^0_{-1}\rangle + |\mathrm{LG}^1_{+1}\rangle - |\mathrm{LG}^1_{-1}\rangle)/2\}$ and (b) $\{|\mathrm{LG}^0_{+1}\rangle, |\mathrm{LG}^0_{-1}\rangle, |\mathrm{LG}^1_{+1}\rangle, |\mathrm{LG}^1_{-1}\rangle\}$. P_i are the optimized pump modes to selectively upconvert signal S_i, where $i = 1$–4.

manipulation by changing the delay of the signal pulses with respect to the pump pulses. The upconverted photons are detected as a function of the temporal delay scanned by the programmable ODL between the synchronous signal and pump pulses. In Fig. 9, we define signal modes in three dimensions, x, y, and t, and consider six signal modes. The spatial profile of these six signals are S_1: $(\mathrm{LG}^0_{-1} + \mathrm{LG}^0_1)/\sqrt{2}$, S_2: $(\mathrm{LG}^0_{-1} - \mathrm{LG}^0_1)/\sqrt{2}$, S_3: $(\mathrm{LG}^0_{-1} - \mathrm{LG}^0_1)/\sqrt{2}$, S_4: $(\mathrm{LG}^0_{-1} - i\mathrm{LG}^0_1)/\sqrt{2}$, S_5: LG^0_{-1}, and S_6: LG^0_1, and the corresponding temporal delays are $t_0 = 0$, 5, 20, 15, 10, and 25 ps, respectively. The optimized pump P_1 (P_5) is designed to selectively upconvert S_1 (S_5) and suppress the others. The selectivities for P_1 and P_5 are 15 and 14 dB on average, respectively. These selectivities can further improve with other efficient adaptive optimization methods [43,50,51].

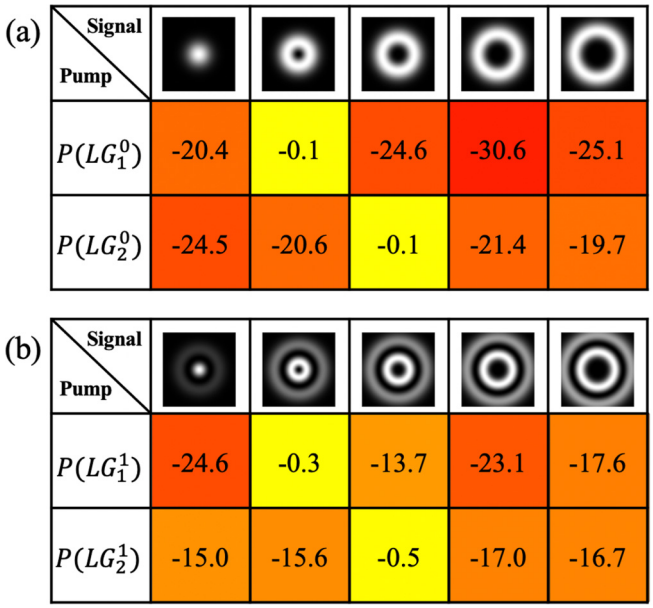

FIG. 8. Spatial mode-selective upconversion of the signal modes with optimized superposition of the pump LG modes. The values in the table are the normalized SF output $\bar{N}$ dB, which are evaluated from Eq. (6). Five signal modes from left to right are (a) $\{\mathrm{LG}^0_0, \mathrm{LG}^0_1, \mathrm{LG}^0_2, \mathrm{LG}^0_3, \mathrm{LG}^0_4\}$, and (b) $\{\mathrm{LG}^1_0, \mathrm{LG}^1_1, \mathrm{LG}^1_2, \mathrm{LG}^1_3, \mathrm{LG}^1_4\}$, respectively.

V. DISCUSSION

In the current setup, the spatial mode shaping of the pump is provided by the SLM and the temporal shaping is realized by the time delay. In the future, an optical arbitrary waveform generator based on spectral line-by-line pulse shaping can be utilized to arbitrarily manipulate the amplitude and phase profiles of the time-frequency modes [43]. This can improve the selectivity of the signal modes by preparing the

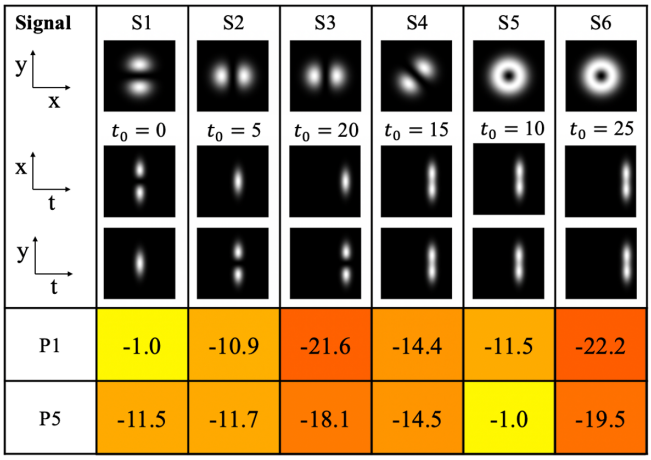

FIG. 9. Spatiotemporal selectivity of the signal modes with optimized pump modes. The values in the table are the normalized SF output $\bar{N}$ dB. The spatial modes of these six signals are S_1: $(\mathrm{LG}^0_{-1} + \mathrm{LG}^0_1)/\sqrt{2}$, S_2: $(\mathrm{LG}^0_{-1} - \mathrm{LG}^0_1)/\sqrt{2}$, S_3: $(\mathrm{LG}^0_{-1} - \mathrm{LG}^0_1)/\sqrt{2}$, S_4: $(\mathrm{LG}^0_{-1} - i\mathrm{LG}^0_1)/\sqrt{2}$, S_5: LG^0_{-1}, and S_6: LG^0_1. The corresponding temporal delays t_0 of the signals are 0, 5, 20, 15, 10, and 25 ps, respectively.

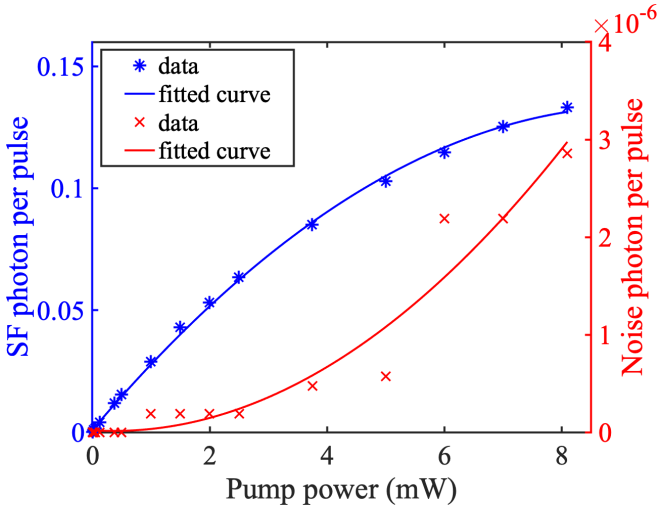

FIG. 10. Experimentally measured SF photon counts (blue asterisk) and background noise photon counts (red cross) vs average pump power. The solid red and blue curves are the corresponding fits.

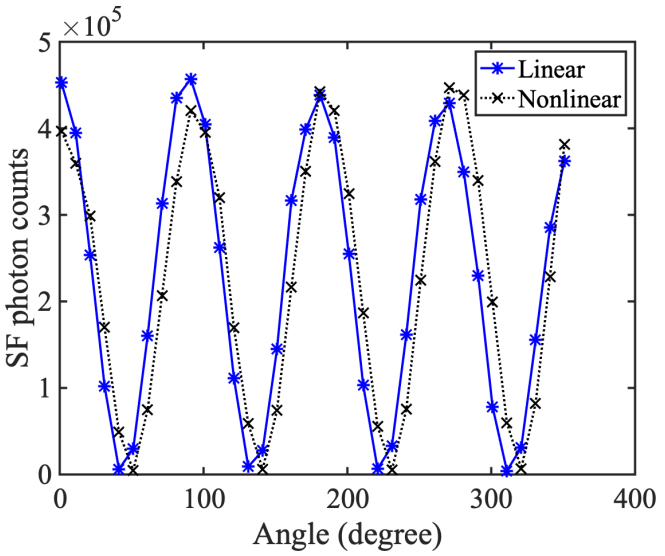

FIG. 11. SF photon counts vs polarization rotation of the pump half-wave plate (θ_p) with respect to the crystal. θ_{SF} is the polarization rotation of the half-wave plate with respect to the visible PBS.

pump pulses in the optimized amplitude and phase profiles in time. Merging the selectivity in spatial and time-frequency modes will realize the full advantage of spatiotemporal mode-selective QFC. We envision that spatiotemporal mode selectivity will be effective against channel noise in both measurable spatial and temporal dimensionalities, thus enabling robust and realistic entanglement distribution with high-dimensional encoding [52] with a minimum trade-off. Note that the selectivity and conversion efficiency of the QFC can be improved while suppressing its intrinsic noise level by using a longer nonlinear crystal with a well-defined phase matching profile [16]. The signal-to-noise ratio in our current nonlinear crystal is shown in Fig. 10. To characterize the quantum noise generated by the nonlinear frequency conversion process in our experiment, we measured the upconverted SF photon per pulse and background noise photon per pulse versus average pump power. The noise photon observed in Fig. 10 indicates that the noise photon counts per pulse is $\sim 10^{-6}$, less than the noise level attained in LN waveguides [53]. The background noise photons could be generated by the pump field due to unwanted second-harmonic and spontaneous parametric downconversion processes [53,54]. In this work, the background noise ~46 dB lower than the upconverted SF photons.

We can also incorporate polarization degrees of freedom to extend the mode-selective QFC [18,29]. The preliminary measurements in the polarization degree of freedom are shown in Fig. 11. We measured the SF photon counts with respect to the rotation of the half-wave plates θ_p (black dotted curve) and θ_{SF} (blue solid curve). In both cases, we record the photon counts using the same visible APD detector. It shows that the visibility of the SF photon counts in linear and nonlinear cases are 0.9832 and 0.9804, respectively (see the Appendix). Incorporating polarization DOF would extend the dimensionality of our mode-selective QFC [18,29,55].

Owing to excellent selectivity among traverse spatial modes, our technique can be used for measurement of the traverse spatial mode joint probability distribution of a biphoton state produced in spontaneous parametric downconversion [56,57] by performing a mode-selective measurement on the photon pair separately. Subsequently, this will allow one to directly quantify and certify high-dimensional entanglement in a traverse spatial mode.

VI. CONCLUSION

We have demonstrated a high-dimensional mode-selective QFC in the spatiotemporal DOF. Our experimental results showed that a high-dimensional QFC can be realized with high extinction (up to 30 dB) by selectively upconverting the signal modes using an optimized pump. This technique is potentially useful for multifold quantum applications [58,59] such as long-distance quantum communication, quantum key distribution (QKD), quantum state tomography, and so on. In the future, it could be extended to other DOF to increase the information capacity of the quantum signals.

ACKNOWLEDGMENTS

This research was supported in part by the National Science Foundation (Grant No. 1842680) and in part by the Earth Science Technology Office, NASA, through the Instrument Incubator Program.

APPENDIX

1. Spatial modes

The Laguerre-Gaussian (LG) modes can be written in the cylindrical coordinates as

$$\mathrm{LG}_l^p(r,\phi,z) = \frac{C_{lp}}{w}\left(\frac{r\sqrt{2}}{w}\right)^{|l|} L_{|l|}^p\left(\frac{2r^2}{w^2}\right)\exp(-il\phi) \times \exp\left(i\zeta - ikz - \frac{ikr^2}{2R} - \frac{r^2}{w^2}\right), \quad \text{(A1)}$$

where $\phi = \arctan(y/x)$ is the azimuthal coordinate, $C_{lp} = \sqrt{\frac{2p!}{\pi(p+|l|)!}}$ is a normalization constant, and $\{L^p_{|l|}\}$ are the generalized Laguerre polynomials with the azimuthal mode index l and the radial index p. The LG modes can be expressed as the superposition of Hermite-Gaussian (HG) modes and vice versa [60]. The LG^p_l modes with the angular mode number $l = n - m$ and radial mode number $p = \min(m, n)$. These can be written as

$$\mathrm{LG}^0_{\pm 1} = \frac{1}{\sqrt{2}}(\mathrm{HG}_{01} \pm i\mathrm{HG}_{10}), \tag{A2}$$

$$\mathrm{HG}_{01}(\theta) = \frac{1}{\sqrt{2}}\left(\mathrm{LG}^0_{+1}e^{-i\theta} + \mathrm{LG}^0_{-1}e^{i\theta}\right), \tag{A3}$$

where θ is the angle of rotation of the coordinate frame from (x, y) to (x', y').

2. Polarization degree of freedom

Visibility can be evaluated as

$$V = \frac{C_{\max} - C_{\min}}{C_{\max} + C_{\min}}, \tag{A4}$$

where $C_{\max}$ and $C_{\min}$ are the maximum and minimum number of SF photon counts.

[1] T. Liu, Q.-P. Su, J.-H. Yang, Y. Zhang, S.-J. Xiong, J.-M. Liu, and C.-P. Yang, Transferring arbitrary d-dimensional quantum states of a superconducting transmon qudit in circuit QED, Sci. Rep. **7**, 7039 (2017).

[2] D.-S. Ding, W. Zhang, S. Shi, Z.-Y. Zhou, Y. Li, B.-S. Shi, and G.-C. Guo, High-dimensional entanglement between distant atomic-ensemble memories, Light: Sci. Appl. **5**, e16157 (2016).

[3] D.-S. Ding, W. Zhang, Z.-Y. Zhou, S. Shi, J.-s. Pan, G.-Y. Xiang, X.-S. Wang, Y.-K. Jiang, B.-S. Shi, and G.-C. Guo, Toward high-dimensional-state quantum memory in a cold atomic ensemble, Phys. Rev. A **90**, 042301 (2014).

[4] C. Li, Y.-K. Wu, W. Chang, S. Zhang, Y.-F. Pu, N. Jiang, and L.-M. Duan, High-dimensional entanglement between a photon and a multiplexed atomic quantum memory, Phys. Rev. A **101**, 032312 (2020).

[5] A. Sit, F. Bouchard, R. Fickler, J. Gagnon-Bischoff, H. Larocque, K. Heshami, D. Elser, C. Peuntinger, K. Günthner, B. Heim, C. Marquardt, G. Leuchs, R. W. Boyd, and E. Karimi, High-dimensional intracity quantum cryptography with structured photons, Optica **4**, 1006 (2017).

[6] A. Singh, Q. Li, S. Liu, Y. Yu, X. Lu, C. Schneider, S. Höfling, J. Lawall, V. Verma, R. Mirin, S. W. Nam, J. Liu, and K. Srinivasan, Quantum frequency conversion of a quantum dot single-photon source on a nanophotonic chip, Optica **6**, 563 (2019).

[7] E. Otte, I. Nape, C. Rosales-Guzmán, C. Denz, A. Forbes, and B. Ndagano, High-dimensional cryptography with spatial modes of light: tutorial, J. Opt. Soc. Am. B **37**, A309 (2020).

[8] N. Gisin, G. Ribordy, W. Tittel, and H. Zbinden, Quantum cryptography, Rev. Mod. Phys. **74**, 145 (2002).

[9] Z. Xie, T. Zhong, S. Shrestha, X. Xu, J. Liang, Y.-X. Gong, J. C. Bienfang, A. Restelli, J. H. Shapiro, F. N. C. Wong, and C. W. Wong, Harnessing high-dimensional hyperentanglement through a biphoton frequency comb, Nat. Photonics **9**, 536 (2015).

[10] M. Erhard, R. Fickler, M. Krenn, and A. Zeilinger, Twisted photons: New quantum perspectives in high dimensions, Light: Sci. Appl. **7**, 17146 (2018).

[11] Y.-H. Luo, H.-S. Zhong, M. Erhard, X.-L. Wang, L.-C. Peng, M. Krenn, X. Jiang, L. Li, N.-L. Liu, C.-Y. Lu, A. Zeilinger, and J.-W. Pan, Quantum Teleportation in High Dimensions, Phys. Rev. Lett. **123**, 070505 (2019).

[12] F. Brandt, M. Hiekkamäki, F. Bouchard, M. Huber, and R. Fickler, High-dimensional quantum gates using full-field spatial modes of photons, Optica **7**, 98 (2020).

[13] X.-M. Hu, C. Zhang, B.-H. Liu, Y. Cai, X.-J. Ye, Y. Guo, W.-B. Xing, C.-X. Huang, Y.-F. Huang, C.-F. Li, and G.-C. Guo, Experimental High-Dimensional Quantum Teleportation, Phys. Rev. Lett. **125**, 230501 (2020).

[14] X.-M. Hu, W.-B. Xing, B.-H. Liu, Y.-F. Huang, C.-F. Li, G.-C. Guo, P. Erker, and M. Huber, Efficient Generation of High-Dimensional Entanglement through Multipath Down-Conversion, Phys. Rev. Lett. **125**, 090503 (2020).

[15] Y.-P. Huang and P. Kumar, Mode-resolved photon counting via cascaded quantum frequency conversion, Opt. Lett. **38**, 468 (2013).

[16] P. Manurkar, N. Jain, M. Silver, Y.-P. Huang, C. Langrock, M. M. Fejer, P. Kumar, and G. S. Kanter, Multidimensional mode-separable frequency conversion for high-speed quantum communication, Optica **3**, 1300 (2016).

[17] P. Kumar, Quantum frequency conversion, Opt. Lett. **15**, 1476 (1990).

[18] F. Kaiser, P. Vergyris, A. Martin, D. Aktas, M. P. D. Micheli, O. Alibart, and S. Tanzilli, Quantum optical frequency up-conversion for polarisation entangled qubits: Towards interconnected quantum information devices, Opt. Express **27**, 25603 (2019).

[19] T. van Leent, M. Bock, R. Garthoff, K. Redeker, W. Zhang, T. Bauer, W. Rosenfeld, C. Becher, and H. Weinfurter, Long-Distance Distribution of Atom-Photon Entanglement at Telecom Wavelength, Phys. Rev. Lett. **124**, 010510 (2020).

[20] M. Bock, P. Eich, S. Kucera, M. Kreis, A. Lenhard, C. Becher, and J. Eschner, High-fidelity entanglement between a trapped ion and a telecom photon via quantum frequency conversion, Nat. Commun. **9**, 1998 (2018).

[21] A. P. VanDevender and P. G. Kwiat, Quantum transduction via frequency upconversion (invited), J. Opt. Soc. Am. B **24**, 295 (2007).

[22] O. J. Farías, V. D'Ambrosio, C. Taballione, F. Bisesto, S. Slussarenko, L. Aolita, L. Marrucci, S. P. Walborn, and F. Sciarrino, Resilience of hybrid optical angular momentum qubits to turbulence, Sci. Rep. **5**, 8424 (2015).

[23] J. M. Lukens and P. Lougovski, Frequency-encoded photonic qubits for scalable quantum information processing, Optica **4**, 8 (2017).

[24] H.-H. Lu, J. M. Lukens, N. A. Peters, B. P. Williams, A. M. Weiner, and P. Lougovski, Quantum interference and correlation control of frequency-bin qubits, Optica **5**, 1455 (2018).

[25] K. H. Kagalwala, G. Di Giuseppe, A. F. Abouraddy, and B. E. A. Saleh, Single-photon three-qubit quantum logic using spatial light modulators, Nat. Commun. **8**, 739 (2017).

[26] R. Fickler, R. Lapkiewicz, M. Huber, M. P. Lavery, M. J. Padgett, and A. Zeilinger, Interface between path and orbital angular momentum entanglement for high-dimensional photonic quantum information, Nat. Commun. **5**, 4502 (2014).

[27] D. Cozzolino, D. Bacco, B. Da Lio, K. Ingerslev, Y. Ding, K. Dalgaard, P. Kristensen, M. Galili, K. Rottwitt, S. Ramachandran, and L. K. Oxenløwe, Orbital Angular Momentum States Enabling Fiber-Based High-Dimensional Quantum Communication, Phys. Rev. Appl. **11**, 064058 (2019).

[28] G. B. Xavier and G. Lima, Quantum information processing with space-division multiplexing optical fibres, Commun. Phys. **3**, 9 (2020).

[29] S. Liu, C. Yang, Z. Xu, S. Liu, Y. Li, Y. Li, Z. Zhou, G. Guo, and B. Shi, High-dimensional quantum frequency converter, Phys. Rev. A **101**, 012339 (2020).

[30] E. Nagali, F. Sciarrino, F. D. Martini, B. Piccirillo, E. Karimi, L. Marrucci, and E. Santamato, Polarization control of single photon quantum orbital angular momentum states, Opt. Express **17**, 18745 (2009).

[31] E. Karimi, L. Marrucci, C. de Lisio, and E. Santamato, Time-division multiplexing of the orbital angular momentum of light, Opt. Lett. **37**, 127 (2012).

[32] N. Maring, D. Lago-Rivera, A. Lenhard, G. Heinze, and H. de Riedmatten, Quantum frequency conversion of memory-compatible single photons from 606 nm to the telecom C-band, Optica **5**, 507 (2018).

[33] S. Kumar, H. Zhang, S. Maruca, and Y.-P. Huang, Mode-selective image upconversion, Opt. Lett. **44**, 98 (2019).

[34] H. J. Kimble, The quantum internet, Nature (London) **453**, 1023 (2008).

[35] A. Reiserer and G. Rempe, Cavity-based quantum networks with single atoms and optical photons, Rev. Mod. Phys. **87**, 1379 (2015).

[36] J. Liu, I. Nape, Q. Wang, A. Vallés, J. Wang, and A. Forbes, Multidimensional entanglement transport through single-mode fiber, Sci. Adv. **6**, eaay0837 (2020).

[37] M. Allgaier, V. Ansari, L. Sansoni, C. Eigner, V. Quiring, R. Ricken, G. Harder, B. Brecht, and C. Silberhorn, Highly efficient frequency conversion with bandwidth compression of quantum light, Nat. Commun. **8**, 14288 (2017).

[38] T. Xiang, Q.-C. Sun, Y. Li, Y. Zheng, and X. Chen, Single-photon frequency conversion via cascaded quadratic nonlinear processes, Phys. Rev. A **97**, 063810 (2018).

[39] Y. Li, Y. Huang, T. Xiang, Y. Nie, M. Sang, L. Yuan, and X. Chen, Multiuser Time-Energy Entanglement Swapping Based on Dense Wavelength Division Multiplexed and Sum-Frequency Generation, Phys. Rev. Lett. **123**, 250505 (2019).

[40] Y. Tang, K. Li, X. Zhang, J. Deng, G. Li, and E. Brasselet, Harmonic spin–orbit angular momentum cascade in nonlinear optical crystals, Nat. Photonics **14**, 658 (2020).

[41] S. W. Hancock, S. Zahedpour, A. Goffin, and H. M. Milchberg, Free-space propagation of spatiotemporal optical vortices, Optica **6**, 1547 (2019).

[42] A. Chong, C. Wan, J. Chen, and Q. Zhan, Generation of spatiotemporal optical vortices with controllable transverse orbital angular momentum, Nat. Photonics **14**, 350 (2020).

[43] A. Shahverdi, Y. M. Sua, L. Tumeh, and Y.-P. Huang, Quantum parametric mode sorting: Beating the time-frequency filtering, Sci. Rep. **7**, 6495 (2017).

[44] H. Zhang, S. Kumar, and Y.-P. Huang, Mode selective upconversion detection with turbulence, Sci. Rep. **9**, 17481 (2019).

[45] H. Zhang, S. Kumar, and Y.-P. Huang, Super-resolution optical classifier with high photon efficiency, Opt. Lett. **45**, 4968 (2020).

[46] D. V. Reddy and M. G. Raymer, High-selectivity quantum pulse gating of photonic temporal modes using all-optical Ramsey interferometry, Optica **5**, 423 (2018).

[47] P. Rehain, Y. M. Sua, S. Zhu, I. Dickson, B. Muthuswamy, J. Ramanathan, A. Shahverdi, and Y.-P. Huang, Noise-tolerant single photon sensitive three-dimensional imager, Nat. Commun. **11**, 921 (2020).

[48] R. Fickler, R. Lapkiewicz, W. N. Plick, M. Krenn, C. Schaeff, S. Ramelow, and A. Zeilinger, Quantum entanglement of high angular momenta, Science **338**, 640 (2012).

[49] P.-A. Moreau, E. Toninelli, T. Gregory, R. S. Aspden, P. A. Morris, and M. J. Padgett, Imaging Bell-type nonlocal behavior, Sci. Adv. **5**, eaaw2563 (2019).

[50] K. S. Kravtsov, S. S. Straupe, I. V. Radchenko, N. M. T. Houlsby, F. Huszár, and S. P. Kulik, Experimental adaptive Bayesian tomography, Phys. Rev. A **87**, 062122 (2013).

[51] V. Ansari, J. M. Donohue, B. Brecht, and C. Silberhorn, Tailoring nonlinear processes for quantum optics with pulsed temporal-mode encodings, Optica **5**, 534 (2018).

[52] S. Ecker, F. Bouchard, L. Bulla, F. Brandt, O. Kohout, F. Steinlechner, R. Fickler, M. Malik, Y. Guryanova, R. Ursin, and M. Huber, Overcoming Noise in Entanglement Distribution, Phys. Rev. X **9**, 041042 (2019).

[53] H. Fan, Z. Ma, J. Chen, Z. Li, C. Tang, Y. M. Sua, and Y. Huang, Photon conversion in thin-film lithium niobate nanowaveguides: A noise analysis, J. Opt. Soc. Am. B **38**, 2172 (2021).

[54] Y. M. Sua, H. Fan, A. Shahverdi, J.-Y. Chen, and Y.-P. Huang, Direct generation and detection of quantum correlated photons with 3.2 μm wavelength spacing, Sci. Rep. **7**, 17494 (2017).

[55] Z.-C. Ren, Y.-C. Lou, Z.-M. Cheng, L. Fan, J. Ding, X.-L. Wang, and H.-T. Wang, Optical frequency conversion of light with maintaining polarization and orbital angular momentum, Opt. Lett. **46**, 2300 (2021).

[56] S. P. Walborn, A. N. de Oliveira, R. S. Thebaldi, and C. H. Monken, Entanglement and conservation of orbital angular momentum in spontaneous parametric down-conversion, Phys. Rev. A **69**, 023811 (2004).

[57] Z. Ibarra-Borja, C. Sevilla-Gutiérrez, R. Ramírez-Alarcón, Q. Zhan, H. Cruz-Ramírez, and A. B. U'Ren, Direct observation of OAM correlations from spatially entangled bi-photon states, Opt. Express **27**, 25228 (2019).

[58] C. Fabre and N. Treps, Modes and states in quantum optics, Rev. Mod. Phys. **92**, 035005 (2020).

[59] X.-M. Hu, W.-B. Xing, C. Zhang, B.-H. Liu, M. Pivoluska, M. Huber, Y.-F. Huang, C.-F. Li, and G.-C. Guo, Experimental creation of multi-photon high-dimensional layered quantum states, npj Quantum Inf. **6**, 88 (2020).

[60] Y. Wang, Y. Chen, Y. Zhang, H. Chen, and S. Yu, Generalised Hermite–Gaussian beams and mode transformations, J. Opt. **18**, 055001 (2016).